

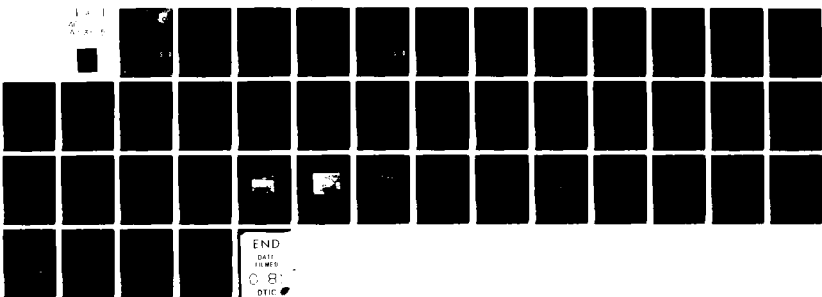
AD-A103 585 DAYTON UNIV OH RESEARCH INST  
AUGER ELECTRON SPECTROSCOPY AND RUTHERFORD BACKSCATTERING STUDY--ETC(U)  
MAY 81 J S SOLOMON F33615-78-C-5102

F/G 11/6

NL

UNCLASSIFIED

AFWAL-TR-81-4010



END  
DATE  
NUMBER  
Q. 8  
DTIC

LEVEL

16 AFWAL TR-81-4010

AD A103585



1 AUGER ELECTRON SPECTROSCOPY AND RUTHERFORD BACKSCATTERING STUDIES  
OF COPPER IN 2024-T<sub>3</sub> ALUMINUM FOLLOWING ELECTROCHEMICAL ANODIZATION  
IN PHOSPHORIC ACID

16 J. S. SOLOMON

UNIVERSITY OF DAYTON RESEARCH INSTITUTE  
300 COLLEGE PARK AVENUE  
DAYTON, OHIO 45469

May 1981

1 TECHNICAL REPORT AFWAL-TR-81-4010

Interim Report for Period August 1979 - Sep 1980

16 3-11-21  
17 02

12 441 DTIC  
S ELECTED SEP 2 1981 D  
D

Approved for public release; distribution unlimited

DTIC FILE COPY

MATERIALS LABORATORY  
AIR FORCE WRIGHT AERONAUTICAL LABORATORIES  
AIR FORCE SYSTEMS COMMAND  
WRIGHT-PATTERSON AIR FORCE BASE, OHIO 45433

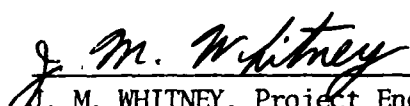
87 87 87 9-2-1981

NOTICE

When Government drawings, specifications, or other data are used for any purpose other than in connection with a definitely related Government procurement operation, the United States Government thereby incurs no responsibility nor any obligation whatsoever; and the fact that the Government may have formulated, furnished, or in any way supplied the said drawings, specifications, or other data, is not to be regarded by implication or otherwise as in any manner licensing the holder or any other person or corporation, or conveying any rights or permission to manufacture, use, or sell any patented invention that may in any way be related thereto.

This report has been reviewed by the Office of Public Affairs (ASD/PA) and is releasable to the National Technical Information Service (NTIS). At NTIS, it will be available to the general public, including foreign nations.

This technical report has been reviewed and is approved for publication.



J. M. WHITNEY, Project Engineer  
Mechanics & Surface Interactions Branch  
Nonmetallic Materials Division



S. W. TSAI, Chief  
Mechanics & Surface Interactions Branch  
Nonmetallic Materials Division

FOR THE COMMANDER



F. D. CHERRY, Chief  
Nonmetallic Materials Division

"If your address has changed, if you wish to be removed from our mailing list, or if the addressee is no longer employed by your organization please notify AFWAL/MLBM, W-PAFB, Ohio 45433 to help us maintain a current mailing list.

Copies of this report should not be returned unless return is required by security considerations, contractual obligations, or notice on a specific document.

**DD FORM 1473 EDITION OF 1 NOV 65 IS OBSOLETE**

SECURITY CLASSIFICATION OF THIS PAGE (When Data Entered)

20.

presence of copper at the oxide-metal interface is shown to affect oxide morphology.

FOREWORD

This technical report was prepared by J.S.Solomon of the University of Dayton Research Institute, Dayton, Ohio. The work was initiated under Project 2419 "Nonmetallic and Composite Materials", and was administered by the Air Force Wright Aeronaautical Laboratories, Air Force Systems Command, Wright-Patterson Air Force Base, Ohio.

This report covers work conducted inhouse during the period August 1979 to September 1980.

The author is very grateful to Professor A. Cachard of the Department of Material Physics, Claude Bernard University, Lyon, France for his contributions to the RBS experimental work and data interpretation.

Accession For	
NTI - Travel	
DTIC - DMR	
Unannounced	
Justified	
By _____	
Distribution/ _____	
Availability Codes	
Dist	Avail and/or
	Special
A	

DTIC  
ELECTED  
S SEP 2 1981 D  
D

## TABLE OF CONTENTS

SECTION	PAGE
I INTRODUCTION	1
II EXPERIMENTAL	2
1. Specimen Preparation	2
2. Method of Analysis	2
A. Auger Electron Spectroscopy	2
B. Rutherford Backscattering	5
III RESULTS	8
IV DISCUSSION	11
V CONCLUSIONS	13
REFERENCES	15
APPENDIX	19

## LIST OF ILLUSTRATIONS

FIGURE	PAGE
1 Depth resolution $\Delta t/t$ (where t is sputtering time in minutes) versus anodic oxide thickness sputtered on Al and 2024-T3 anodized in room temperature 1.0M $H_3PO_4$ at 10 volts	22
2 SEM micrograph of oxides on aluminum anodized in room temperature 0.05M $H_3PO_4$ at 60 volts for 1 hour	23
3 SEM micrograph of oxide on 2024-T3 anodized in room temperature 1.0M $H_3PO_4$ at 10 volts for 20 minutes	24
4 Illustration of the penetration, backscattering and the subsequent energy loss of a high energy ion in a solid target material	25
5 Illustration of an ideal RBS spectrum from a thin anodic oxide on a $H_3PO_4$ anodized aluminum target	26
6 AES spectra of "as received" (a) and equilibrium sputtered (b) 2024-T3 aluminum	27
7 AES spectrum from Oakite-etched 2024-T3 surface	28
8 AES spectrum of $H_3PO_4$ anodized 2024-T3	29
9 Oxygen, aluminum and copper Auger Sputter profiles of the surface oxide layer of Oakite deoxidized 2024-T3 aluminum	30
10 Auger sputter profiles of copper in anodic oxide films on Oakite-etched 2024-T3 anodized at 10 volts in room temperature 1.0M $H_3PO_4$	31
11 Auger sputter profiles of oxygen, aluminum and copper of the surface oxide layer on non-etched 2024-T3 anodized at 10 volts for 1 minute in room temperature 1.0M $H_3PO_4$	32
12 Oxide film thickness on aluminum and 2024-T3 plotted as a function of anodization time at 10 volts in room temperature 1.0M $H_3PO_4$	33

13 RBS spectrum from Oakite etched 2024-T3 with a 2 MeV  ${}^4\text{He}^+$  beam 34

14 RBS spectrum from Oakite etched 2024-T3 anodized in room temperature 1.0M  $\text{H}_3\text{PO}_4$  at 10 volts for 20 minutes obtained using a 2 MeV  ${}^4\text{He}^+$  beam 35

15 RBS spectra of the Cu and P peaks from Oakite etched 2024-T3 anodized in room temperature 1.0M  $\text{H}_3\text{PO}_4$  at 10 volts for times in minutes, as specified for each spectra, using a 2 MeV  ${}^4\text{He}^+$  beam 36

LIST OF TABLES

TABLE	PAGE
1 Sputter rates for anodic oxides on Al and 2024-T3 using a 2keV $3.0 \mu\text{A/mm}^2$ Argon ion beam	19
2 $dE/dx$ ( $\text{keV}\cdot\text{ug}^{-1} \cdot \text{cm}^2$ ) values for 2 MeV ${}^4\text{He}^+$ ions in Aluminum Copper and $\text{Al}_{0.98}\text{Cu}_{0.02}$	20
3 Rutherford Backscattering data from Oakite etched and 10 volt 1.0M $\text{H}_3\text{PO}_4$ anodized 2024-T3 with a 2 MeV ${}^4\text{He}^+$ beam	21

## INTRODUCTION

Aircraft structural materials, such as 2024 aluminum are being used increasingly in adhesively bonded structures. When an aluminum alloy is to be adhesively bonded to itself or to other metals, chemical pretreatment is necessary. The pretreatment must be tailored to the application of a bonded structure and the desired performance and life time requirements. At present, the surface preparation of aluminum alloys for adhesive bonding receiving the highest interest in the Aircraft Industry and the Air Force is chemical deoxidation followed by phosphoric acid electrochemical anodization (reference 1-3).

When aluminum is anodized in an aggressive electrolyte, such as  $H_3PO_4$ , the resulting anodic oxide has a porous structure (reference 4-6). Previous studies (reference 4,5,7) have shown that this anodic oxide film consists of two distinct regions: a thin, dense barrier oxide layer located at the oxide-metal interface and a thicker porous oxide layer situated on top of the barrier layer. Pore formation and subsequent oxide growth on aluminum has been explained in terms of field-assisted dissolution of the barrier layer (reference 8). As the initial oxide layer is formed and dissolved, the current becomes concentrated in thinner areas (reference 5) through which  $Al^{+3}$  migrates and reacts with  $OH^-$  and  $O^{-2}$  to continually form new oxide. Oxide growth then proceeds inward forming well defined columns.

The anodic oxide growth mechanism for 2024-T3 is essentially the same as aluminum. However, the morphology of the oxide layer differs from that of the pure metal in that it does not have the well defined characteristic columnar structure (reference 9). Furthermore, the alloy is not homogeneous, but contains intermetallic compounds, such as  $CuAl_2$ , and microconstituents, such as Al-Cu-Mg, which have different oxidation or dissolution rates than the Al-Cu

solid solution. When inclusions such as these are present at or near the surface, discontinuities within the anodic oxide layer can result (reference 10).

Because the chemical and physical properties of the anodic oxide layer are vital to the strength and durability characteristics of adhesive bonded structures of aluminum alloys, their control and predictability throughout anodization is extremely important. For example, copper containing aluminum alloys are highly vulnerable to environmental corrosive attack. While an anodic oxide surface layer does offer limited corrosion resistance (reference 9), the amount of protection is diminished with thinner films (reference 11) or the enrichment of copper at the oxide metal interface (reference 12).

This report discusses the effects of anodization on the distribution of copper within the oxide and oxide-metal interface and its possible influence on anodic oxide morphology. The anodized pieces were characterized by Auger Electron Spectroscopy (AES), Auger Sputter Profile Analysis (ASPA), and Rutherford Backscattering (RBS).

## II EXPERIMENTAL

### 1. Specimen Preparation

Circular pieces of 2024-T3 aluminum approximately 5 cm in diameter x 0.2 cm thick were first degreased with acetone. One set was then deoxidized in Oakite (reference 13) for 15 minutes and rinsed in distilled H<sub>2</sub>O. The deoxidized pieces were anodized at 10 volts constant potential in a room temperature constant circulation bath of 1.0 M H<sub>3</sub>PO<sub>4</sub> for times of 1,3,5,10,20,60, and 120 minutes. After anodization the specimens were rinsed with distilled H<sub>2</sub>O and hot air dried.

### 2. Method of Analysis

#### A. Auger Electron Spectroscopy (AES)

AES is an analytical technique which is based on the radiationless de-excitation of an excited atom by the emission of electrons. It is a surface sensitive technique in that the emitted electrons come only from the first few layers of atoms at a solid-vacuum interface. The Auger instrumentation and data handling scheme used in this work were previously described (reference 14). A coaxial electron gun which was operated at 4 keV with a current density of  $0.5\mu\text{A}/\text{mm}^2$ , was used to provide high energy excitation of the specimen.

When an ion beam is used to etch away surface layers at controlled rates while AES data is being recorded, elemental depth profiles can be constructed. The ion beam used for sputter profiling in this work was generated with a Physical Electronics Industries model 94-191 Sputter Ion Gun which was operated with a beam energy of 2keV and an ion current density of approximately  $3\mu\text{A}/\text{mm}^2$  in a partial pressure of argon of  $6.6 \times 10^{-3}$  Pa.

Thickness or depth measurements based on Auger sputter profile analysis (ASPA) data require a knowledge of elemental sputter rates in a particular matrix in order to relate sputter time to depth sputtered. In theory one should be able to determine the rate for anodic aluminum oxide sputter time to reach the oxide-metal interface of anodized specimens whose anodic film thickness were characterized beforehand by such techniques as ellipsometry or scanning electron spectroscopy (SEM). However, even with known oxide thickness standards there still remains uncertainties with regards to the exact location of an oxide-metal interface if, for example, there is a region of oxide and metal mixing near the interface which would broaden the interface over several nanometers thickness.

In this work sputter rates were determined from profile data sputter times required to reach the oxide-metal interface chosen to be the average of the times to reach the artifact minimum in Al<sub>KLL</sub> (reference 15) and the mid-

point of the negative slope of the oxygen profile between the 84% and 16% levels.

Because the morphology and density of an anodic oxide are very sensitive to a number of anodization parameters the sputter rate for electrochemically grown aluminum oxide may differ for various anodization conditions. Therefore, sputter rates were determined for the metal and 2024-T3 anodized in a number of electrolytes at various anodization conditions. Table I shows the sputter rates from phthalic acid anodized aluminum (non-porous oxide structure), 1.0M  $H_3PO_4$  anodized Al and 2024-T3 and 1.0M  $H_2SO_4$  anodized 2024-T3. The  $H_3PO_4$  and  $H_2SO_4$  anodizations were performed at a 10 volt constant potential. The sputtering was done with a 2keV,  $3\mu A/mm^2$  Ar ion beam.

As shown in Table 1, the sputter rates differ considerably between oxides formed under different anodic conditions. The rate for the more dense oxide formed in phthalic acid was more like that previously reported for  $Al_2O_3$  (reference 16,17) while those for the porous oxides are much greater, reflecting the less dense nature of their structure.

The sputter rate of the alloy anodized in  $H_3PO_4$  increases with oxide thickness. The reason is related to the competing mechanism of growth and electrolyte dissolution and the limit to thickness when an equilibrium between these mechanisms is reached. Thicker films are formed with longer anodization times and thus longer exposures to the electrolyte. This results in less dense structures and thus higher sputter rates. Because the alloy has a lower anodization efficiency than the pure metal the ultimate anodic oxide thickness for a particular set of anodization conditions is less for the alloy. Consequently, at the conditions listed in Table 1, the oxide growth on the metal and alloy anodized in  $H_2PO_4$  were linear with anodization time but the growth on the alloy was approaching

a limiting thickness.

Another serious problem with the use of ASPA to characterize interfacial regions is the broadening effects on the sputter profile contours representing an interface due to poor depth resolution ( $\Delta t/t$ ). Mathieu and Lendolt reported an interfacial width in terms of sputter time ( $\Delta t$ ) for a nonporous type anodic  $\text{Al}_2\text{O}_3$ -Al of approximately 30% of total thickness using a 3keV ion beam (reference 16).

Figure 1 contains plots of  $\Delta t/t$  versus oxide thickness, as defined by Kirschner and Etzkorn (reference 18), obtained from oxygen profiles from 1.0M  $\text{H}_3\text{PO}_4$  anodized Al and 2024-T3. The difference in the respective levels ( $\text{Al} \approx 35\%$ ,  $2024-\text{T3} \approx 55\%$ ) of  $\Delta t/t$  for films thicker than 100nm, is most probably related to the difference in the respective oxide layer textures (reference 19,20), especially near the interface. As shown in Figures 2 and 3 the anodic film on Al has a uniform and non-porous layer between the well defined columnar oxide layer and metal substrate while the texture of the oxide layer on 2024-T3 is rougher with no evidence of an intermediate non-porous layer.

As a consequence of the relatively poor depth resolution of 55% for 2024-T3, interfacial features less than 55 nanometers in thickness in a specimen with a 100 nanometer thick oxide film cannot be characterized by ASPA with a high degree of confidence.

#### B. Rutherford Backscattering (RBS)

Ion backscattering spectroscopy makes use of the energy loss suffered by the elastic collision of a probing light element ion with a heavier atom in a target material. The information provided by this technique primarily concerns atomic concentration and distribution but not chemical. When low energy ions (keV) are used the technique is surface sensitive (reference 21) and is referred to as ion scattering spectroscopy. High energy

backscattering (meV), commonly referred to as Rutherford Backscattering or RBS, is better suited for thin film and bulk analyses.

In this work, Rutherford backscattering was performed using a 2 MeV  ${}^4\text{He}^+$  ion beam produced with a Van de Graaff generator. The backscattered ions were collected by a solid state detector at a scattering angle of  $\theta = 160^\circ$  measured against the forward direction of the incident beam. The energy resolution of the detector was such that the value for  $\frac{dE}{dx}$  (in keV/ $\mu\text{g}/\text{cm}^2$ ) for  ${}^4\text{He}^+$  ions was subject to an error of  $\pm 5\%$ , or a depth resolution of 20 nanometers.

Because of the need for a high energy generator the technique is not commonly used (reference 22). Detailed discussions of this technique can be found elsewhere (reference 22,23) therefore a cursory treatment is presented which describes how calculations of parameters needed for determining the concentration and distribution of copper in anodized 2024-T3 were made.

The loss of energy of the probing ion at a depth  $x$  in the specimen is given by

$$\Delta E = [S] \cdot x$$

where  $S$  is the backscattering energy loss factor.  $[S]$  is determined by the expression

$$[S] = \left[ \frac{k}{\cos\theta_1} \cdot \frac{dE}{dx} \Big|_i + \frac{1}{\cos\theta_2} \cdot \frac{dE}{dx} \Big|_o \right]$$

where  $\theta$  is the scattering angle,  $\frac{dE}{dx}|_i$  is the energy change during inward penetration,  $\frac{dE}{dx}|_o$  is the energy change during outward movement of the scattered ion, and  $k$  is the kinematic factor which is related to the mass of the target material by the expression

$$k_{M_2} = \left\{ \frac{M_1 \cos\theta + \sqrt{M_2^2 - M_1^2 \sin^2\theta}}{M_1 + M_2} \right\}^2$$

where  $M_1$  and  $M_2$  are the atomic masses of the probing ion and target material, respectively. The process involving the above parameters is illustrated in Figure 4.

The changes of energy during penetration and escape from the target are given by (x)  $\lim_{\Delta x \rightarrow 0} \frac{\Delta E_i}{\Delta x} = \frac{dE}{dx}$

where  $E_i$  is the initial energy of the probing ion. Based on reported  $k^2$  values of 0.560 for aluminum and 0.783 for copper (reference 26) values for  $\frac{dE}{dx}$  were calculated for pure aluminum, copper and an  $Al_{0.98}Cu_{0.02}$  solid solution and are listed in Table 2. A 2% copper solution was chosen since that is the nominal bulk concentration of 2024-T3. The  $\frac{dE}{dx}$  value for  $Al_{0.98}Cu_{0.02}$  was calculated with the assumption that the total change in energy is dependent on an additive contribution by both elements according to:

$$\frac{dE}{dx}_{\text{compound AB}} = \frac{M_A \cdot W_A \cdot \frac{dE}{dx}_A + M_B \cdot W_B \cdot \frac{dE}{dx}_B}{M_A \cdot W_A + M_B \cdot W_B}$$

Using the value of  $\frac{dE}{dx}_{AlCu}$  listed in Table 2 the calculated backscattering factors for copper and aluminum in 2024-T3 are  $1.895 \text{ keV} \cdot \mu^{-1} \cdot \text{cm}^2$  and  $1.791 \text{ keV} \cdot \mu^{-1} \cdot \text{cm}^2$  respectively.

The signal heights in a RBS spectrum for particles scattered from a thin film can be used to determine atomic concentrations. For example Figure 5 represents an ideal RBS spectrum form phosphoric acid anodized aluminum. The aluminum to oxygen height ratios can be expressed as:

$$\frac{H_{Al}}{H_0} = \frac{\sigma_{Al}}{\sigma_0} \frac{[\epsilon]_O^{Al_2 O_3}}{[\epsilon]_{Al}^{Al_2 O_3}} \frac{N_{Al}^{Al_2 O_3}}{N_O^{Al_2 O_3}}$$

where  $\sigma_{Al}$  and  $\sigma_0$  are the effective scattering cross sections for aluminum and oxygen, respectively, and  $N_{Al}^{Al_2 O_3} / N_O^{Al_2 O_3}$  is the atomic concentration ratio for aluminum to oxygen, which in the case of  $Al_2 O_3$  should be 2/3.

The atomic concentration for an element A in a compound AB can be then determined by the following expression:

$$\%A = \frac{H_A^{AB}}{H_A^{AB} + H_B^{AB}} \times 100$$

$$\left( \frac{\sigma_A}{\sigma_B} \right) \left( \frac{[S]_B^{AB}}{[S]_A^{AB}} \right)$$

### III RESULTS

The nominal bulk concentration of magnesium in 2024-T3 aluminum is 1.5 wt.% (reference 24) but because the alloy is subjected to a hot rolling process the surface of 2024-T3 usually contains a magnesium-aluminum oxide layer (reference 25). The AES spectrum from an "as received" 2024-T3 panel in Figure 6a shows it to be a magnesium rich oxide. The spectrum in Figure 6b, which represents the surface of 2024-T3 after the oxide is removed by ion beam sputtering, does not reveal the presence of magnesium, inferring that the hot rolling process depleted bulk magnesium near the surface.

Normally the 2024-T3 panels are subjected to a preanodization chemical deoxidation to remove the magnesium rich surface oxide. The AES spectrum in Figure 7, which was recorded from an Oakite-etched 2024-T3 piece, shows an

aluminum oxide surface depleted of magnesium and containing a trace of copper and elements found in the etching solution (i.e., F, N, S). An FPL etch produced a similar surface chemistry, however the surface topography was slightly rougher.

Following the chemical deoxidation step the alloy was anodized and Figure 8 contains the AES spectrum from the anodized 2024-T3 piece. As seen in Figure 8 AES data shows an absence of alloying elements on the surface. This was generally the case for oxide thicknesses greater than 60 nanometers.

Figure 9 contains the in-depth profiles of oxygen, aluminum, and copper obtained by ASPA from the Oakite etched specimen. The oxide is approximately 5-10 nanometers thick while the copper enrichment zone extending from the oxide-metal interface into the bulk alloy is approximately 36 nanometers thick. Copper enrichment was not observed at the oxide-metal interface of non deoxidized or as received specimens. Magnesium was neither detected throughout the oxide nor in the bulk etched alloy immediately below the oxide-metal interface.

The copper in-depth profiles from Oakite deoxidized alloy specimens which were anodized at 10 volts for 1, 3, 5, and 10 minutes are shown in Figure 10. The profile from the 10 minute anodized specimen as well as those from specimens anodized longer than 10 minutes no longer show a copper enrichment at this interface but a concentration level equal to that in the bulk. The depth distributions of the copper enriched zones in the 1, 3, and 5 minute anodized specimens according to Figure 10 are 34, 59, and 84 nanometers, respectively.

The data in Figures 9 and 10 suggest that copper enrichment can be attributed solely to the chemical deoxidation treatment and subsequent

phosphoric acid anodization depletes copper from the oxide-metal interface. However, the copper profile from a non-etched and anodized specimen shown in Figure 11 suggests that anodization also produces a copper enrichment at this oxide-metal interface, independent of the chemical deoxidation step since, as stated above, copper enrichment was not observed in non-treated specimens. Also, copper was not detected within the anodic oxide layer, regardless of thickness or preanodization treatment.

The decreases in copper with anodization time or oxide thickness (see Figure 12 for the relationships of oxide thickness on 2024-T3 and aluminum to anodization time is 1.0M H<sub>3</sub>PO<sub>4</sub> at 10 volts) is due to the chemical dissolution of copper by the electrolyte (reference 9). However, if anodization produces enrichment as shown in Figure 11 one would always expect the presence of a copper enriched interface. Since ASPA data fails to show this, doubt arises as to the reliability of this technique to detect an enrichment in thicker oxides in light of the 55% depth resolution.

The depth resolution of RBS, unlike ASPA, is a fixed thickness and therefore this technique should be more reliable for characterizing the interface region of the anodized specimens. Figures 13 and 14 contain RBS spectra from an Oakite etched specimen and an etched and 20 minute anodized specimen, respectively. In both cases the copper enriched interface is very evident. The absence of an oxygen peak in Figure 13 shows the surface insensitivity of RBS, especially towards light elements such as oxygen.

Figure 15 contains RBS spectra in the region of 1.2 to 1.8 MeV for specimens etched and anodized for times up to 2 hours. Contrary to the ASPA data, copper interfacial enrichment is evident in all cases. Also evident in Figure 15 is a copper deficient (compared to the bulk level) zone extending

approximately 95 nanometers below the enrichment zone. Table 3 lists the width of the copper enrichment zone and weight percent copper in the bulk and at the interface for each of the anodized specimens. The values listed for the bulk composition are in good agreement for the nominal copper concentration of 4.5 weight per cent listed for the 2024-T3 alloy (reference 24).

From Table 3 it appears that copper reaches a steady state interfacial concentration of approximately 0.1 weight percent above the bulk level at anodization times in excess of 20 minutes. The copper enriched zone is also shown to become increasingly broader with anodization time.

The RBS data in Figure 14 shows the stoichiometry of the anodic oxide to be  $\text{Al}_2\text{O}_3$ . Therefore the anodic oxide thickness on the 20 minute anodized specimen was determined to be 86.1 nanometers, based on  $3.97\text{g}/\text{cm}^3$  for the density of  $\text{Al}_2\text{O}_3$  and a backscattering energy loss factor of  $2.05 \text{ keV}/\mu\text{g}/\text{cm}^2$  (reference 26). Since SEM data showed the same film to be approximately 400 nm thick, the real density of the anodic oxide was  $0.86\text{g}/\text{cm}^3$ .

#### IV DISCUSSION

Oxide growth on aluminum by electrochemical anodization in phosphoric acid is limited by both the increasing current retarding effects of the growing oxide film and the dissolving action of the acid electrolyte. The maximum oxide thickness is reached when the dissolution and growth rates become equal (continued anodization beyond this point only affects surface topography).

The presence of copper in aluminum has considerable effect on oxide growth rates (reference 9, 10 and 27). During anodization of copper containing aluminum alloys such as 2024-T3 there is a constant evolution of oxygen (reference 27, 28) which is probably related to a charge transfer mechanism

involving copper rather than aluminum, resulting in copper dissolution by the electrolyte. The net result is a lower concentration of  $\text{Al}^{+3}$  ions to combine with  $\text{O}^{-2}$  ions to form oxide. The consequence of this is reflected in Figure 12 which contains anodization time versus oxide thickness curves for aluminum and 2024-T3 anodized in 1.0 M  $\text{H}_3\text{PO}_4$  at 10 volts constant potential.

The oxide on 2024-T3 has a limiting thickness of approximately 400 nanometers while growth continues on the pure metal (the maximum thickness on the metal was approximately 1000 nanometers).

An interesting subtlety with the aluminum curve in Figure 12 is its initial lower growth rate and subsequent thinner oxide for the first few minutes of anodization, compared to the alloy. This phenomenon is possibly related to the formation of the so called barrier layer prior to columnar growth, the thickness of which is voltage dependent according to a thickness to voltage ratio of 1 to 2 nanometers per volt (reference 29). This film forms in a very short period of time and causes a very rapid decrease in current density due to its electrical resistivity. Almost instantaneous with its formation the electrolyte begins to nonuniformly dissolve the oxide creating thinner areas (pores) whereupon the oxide grows in a columnar fashion at a faster time dependent rate.

In the case of 2024-T3 (see Figure 3) there is little evidence of barrier layer formation (reference 9). According to Strehblow and Doherty (reference 28) the emission of oxygen during anodization prevents the formation of a continuous oxide film. Therefore, uninhibited at the onset by the formation of a continuous oxide film, current not consumed by copper initially forms oxide on the alloy at a faster overall growth rate than on the pure metal.

Another possible consequence of oxygen evolution due to the presence of copper is the effect on oxide morphology. Oxygen evolution most likely occurs

at surface sites containing higher copper concentrations. Only when the copper concentration at one of these sites is decreased by the formation of a soluable compound can oxide growth begin. On the other hand, if the local copper concentration increases with anodization time oxide growth will be retarded or possibly stopped.

The experimental data presented above suggests that during anodization copper diffuses to the oxide-metal interface where anodic growth is occurring. Strehblow et al reported copper diffusion to the oxide-metal interface at a rate of  $3.5 \times 10^{-8}$  cm/sec during the anodization at Al-0.5%Cu (reference 12). They and others attributed this to the creation of vacancies at the oxide-metal interface (reference 12,30).

Since copper is being replenished at the oxide-metal interface by diffusion, local copper concentrations are constantly changing in a cyclic process of dissolution and diffusion. Consequently, oxide growth does not occur at fixed sites during the duration of anodization and the oxide morphology on the alloy is not one of well defined columns but rather that as shown in Figure 3. This does not take into account the effects of very high levels of copper present in the form of intermetallic compounds which would be randomly present at the oxide-metal interface as the Al-Cu solid solution is consumed.

#### V. CONCLUSIONS

The presence of Cu can significantly affect anodic oxide growth behavior during the electrochemical anodization of 2024-T3 Al in  $H_3PO_4$ . At the onset of anodization the presence of Cu can inhibit the formation of a uniform dense oxide film normally observed in the anodization of the pure metal. The result, compared to the pure metal, is a slightly greater growth rate.

The anodization process results in the bulk diffusion of Cu to the oxide-metal alloy interface where, after a period of time, a steady state enriched concentration zone of Cu is established. This zone broadens with longer anodization time. The steady state enrichment of Cu is the result of the competition between the two time dependent mechanisms of diffusion and electrolyte dissolution. Because of this cyclic process growth rates may vary at local sites which in turn can result in a somewhat different oxide morphology than that produced on the pure metal.

The advantages of phosphoric acid anodization of aluminum for adhesive bonding applications are the built in corrosion resistance offered by the barrier layer and large potential for good mechanical interlocking between adhesive and oxide throughout the oxide film owing to the ability of the adhesive to flow into vacant pore columns. Since the anodic oxide formed on 2024-T3 does not form a continuous uniform layer at this oxide-metal interface it is doubtful if the oxide offers significant corrosion resistance. Also, because of its non-columnar morphology the amount of mechanical interlocking between the oxide and adhesive may be reduced.

This suggests that further research is necessary to evaluate the effects of oxide morphology on adhesive bond performance. By altering electrolyte pH and concentration and other anodization parameters it might be possible to change the anodic oxide morphology on 2024-T3 in such a way as to make it a stronger and more durable bonding medium.

## REFERENCES

1. H.S. Schwartz, J. Appl. Poly. Sci., Appl. Poly. Sym., 32, 65 (1977).
2. G. S. Tabayashi and D. J. Donnelly, "Improvement in Environmental Stability of Bonded Aircraft Structure", Boeing Company Report D6-41517, February (1974).
3. A. U. Bethune, SAMPE Journal, 11, 4 (1975).
4. G. E. Thompson, R. C. Furneau, G. C. Wood, J. A. Richardson, and J. S. Goode, Nature, 272, 433 (1978).
5. J. P. O'Sullivan and G. C. Wood, Proc. Roy. Soc. London A., 317, 511 (1970).
6. J. U. Diggle, T. C. Downie, and C. W. Goulding, Chem. Rev., 69, 365 (1969).
7. J. P. Hoar and N. F. Mote, J. Phys. Chem Solids, 9, 97 (1959).
8. J. P. Hoar and Yakalom, J. Electrochem. Soc., 110, 614 (1963).
9. J. S. Solomon and D. E. Hanlin, Applications of Surface Science, 4, 307 (1980).
10. F. Keller, G. W. Wilcox, M. Tosterud, and C. J. Slunder, Metals and Alloys, 10, 219 (1939).
11. R. C. Spooner, J. Electrochem. Soc., 125, 127 (1978).
12. H.-H. Strehblow, C. M. Mellian-Smith, and W. M. Augustyniak, J. Electrochem. Soc., 125, 915 (1978).
13. Oakite Products of Canada, Ltd., Bramlea, Ontario, Canada.
14. J. S. Solomon and W. L. Baum, J. Vac. Sci. Technol., 12, 375 (1975).
15. J. S. Solomon, Applied Spectroscopy, 30, 46 (1976).
16. H. J. Mathieu and D. Landolt, in Proceedings of the 7th International Vacuum Congress and 3rd International Conference on Solid Surfaces, Vienna 1977, Ed. R. Dobrozemsky, F. Rudenauer, F. Viehbock, and A. Breth, (Dobrozemsky, Vienna, 1977) 2023.

17. R. Kelly and N. Q. Lam, Radiat. Eff., 19, 39 (1973).
18. J. Kirschner and H. W. Etzkorn, in Proceedings of the 7th International Vacuum Congress and 3rd International Conference on Solid Surfaces, Vienna 1977, Ed. R. Dobrozemsky, F. Rudenauer, F. Viehbock, and A. Breth, (Dobrozemsky, Vienna, 1977) 2213.
19. S. Hofmann and J. Erlewein, Thin Solid Films, 43, 275 (1977).
20. H. J. Mathieu, D. E. McClure, and D. Landolt, Thin Solid Films, 38, 281 (1976).
21. David P. Smith, Surface Science, 25, 171 (1971).
22. W. K. Chu, J. W. Mayer and M-A. Nicolet, Backscattering Spectrometry, (Academic Press, New York, 1978).
23. S. V. Campisano, W. K. Chu, G. Foti, J. W. Mayer, M-A. Nicolet, and E. Rimini, in Ion Beam Handbook for Material Analysis, J. W. Mayer and E. Rimini, eds., (Academic Press, 1977) p. 21.
24. Adhesive Bonding (Aluminum Company of America) 1967, p 96.
25. T. Rönnbult, V. Rilby and I. Olefjord, Materials Science and Engineering, 42, 329 (1980).
26. M. Romand, A. Cachard, R. Bador, A Roche, and M. Charbonnier, "Caracterisation par Emission X et Retrodiffusion D'ions de Films Anodiques Formes Sur L'Aluminum" Decision D'Aide: No. 1248, Universite Claude Bernard Lyon 1, October 1978, p.19.
27. G. H. Kissin, B. E. Deal and R. V. Paulson, in The Finishing of Aluminum, ed. G. H. Kissin, (Reinhold Publishing Corp., New York, 1963) p. 13.
28. H.-H. Strehblow and C. J. Doherty, J. Electrochem. Soc., 125, 30 (1978).

29. R. C. Furneau, G. E. Thompson and G. C. Wood, Corrosion Sci., 18, 853 (1978).
30. W. D. Mackintosh, F. Brown, and H. H. Plattner, J. Electrochem. Soc., 121, 1281 (1974).

APPENDIX  
FIGURES AND TABLES

Table 1. Sputter Rates for Anodic Oxides on Al and 2024-T3 Using a 2keV  
3.0 $\mu$ A/mm<sup>2</sup> Argon Ion Beam.

Specimen	Sputter Rate (nm/min)	Thickness Range (nm)
C <sub>6</sub> H <sub>4</sub> (COOH) <sub>2</sub> Al	6.0	Al1
10V 1M H <sub>3</sub> PO <sub>4</sub> Al	18.5	0-1000
10V 1M H <sub>3</sub> PO <sub>4</sub> 2024-T3	14.6	0-100
10V 1M H <sub>3</sub> PO <sub>4</sub> 2024-T3	17.1	100-200
10V 1M H <sub>3</sub> PO <sub>4</sub> 2024-T3	18.0	200
10V 1M H <sub>2</sub> SO <sub>4</sub> 2024-T3	10.0	0-1000

Table 2.  $dE/dx$  (keV $\cdot$ ug $^{-1}\cdot$ cm $^2$ ) Values for 2 MeV  ${}^4\text{He}^+$  ions in Aluminum,  
Copper and  $\text{Al}_{0.98}\text{Cu}_{0.02}$

Material	$E_i = 2\text{MeV}$	$k_{\text{Cu}}^2 E = 1.566\text{MeV}$	$k_{\text{Al}}^2 = 1.120\text{MeV}$
Aluminum	0.986	1.085	1.195
Copper	0.629	0.668	0.699
$\text{Al}_{0.98}\text{Cu}_{0.02}$	0.970	1.066	1.172

Table 3. Rutherford Backscattering Data from Oakite etched and 10 volt  
1.0M H<sub>3</sub>PO<sub>4</sub> Anodized 2024-T3 with a 2 MeV <sup>4</sup>He<sup>+</sup> Beam.

Anodization Time (minutes)	Copper Interfacial Width (nanometers)	Weight percent Copper	
		Bulk	Interface
0	38	4.8	7.0
1	38	4.1	6.3
3	48	4.1	5.0
5	57	4.1	4.6
10	76	4.1	4.5
20	91	3.9	4.1
60	85	4.1	4.2
120	91	4.1	4.2

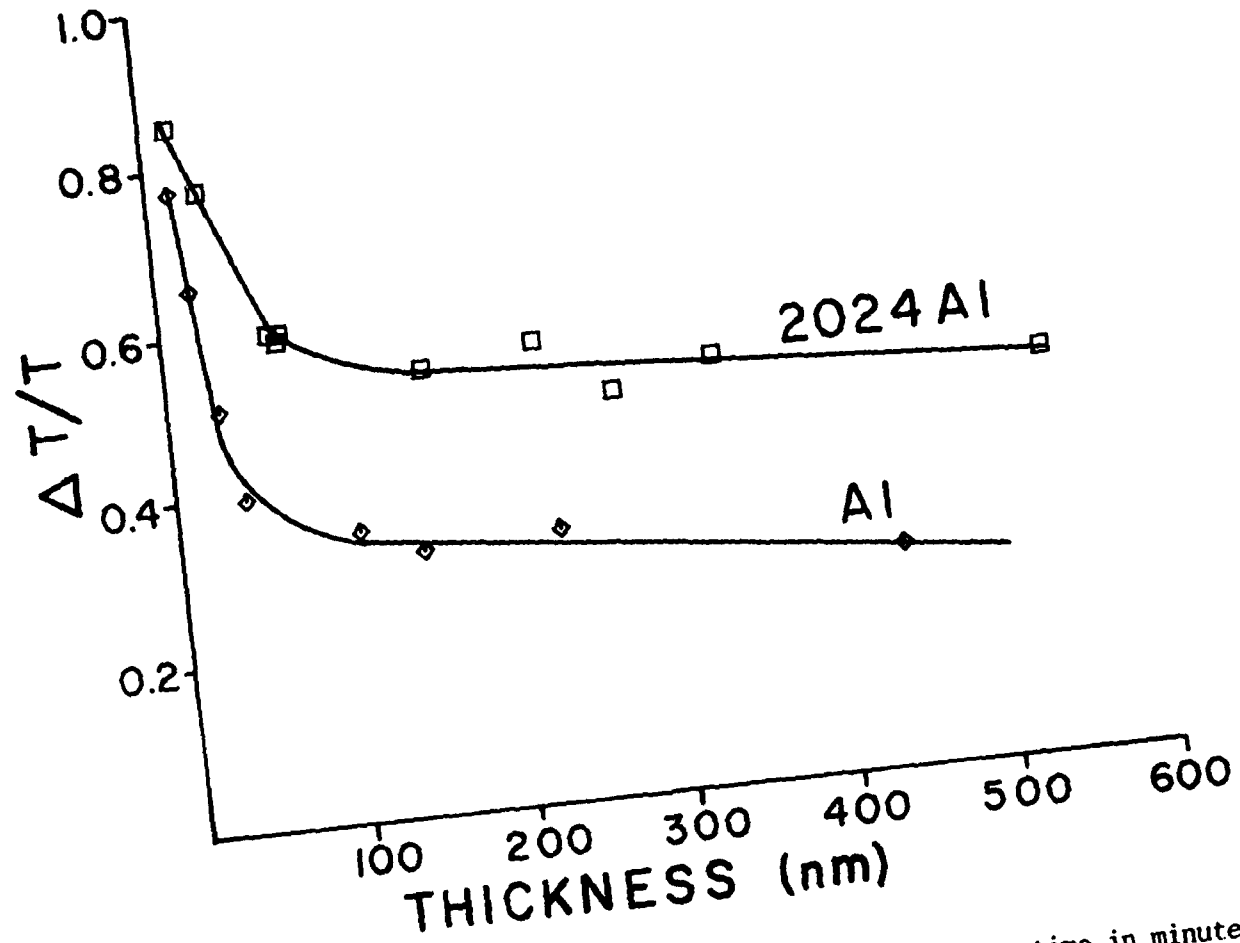


Figure 1 Depth resolution  $\Delta t/t$  (where  $t$  is sputtering time in minutes) versus anodic oxide thickness sputtered on Al and 2024-T3 anodized in room temperature 1.0M  $H_3PO_4$  at 10 volts

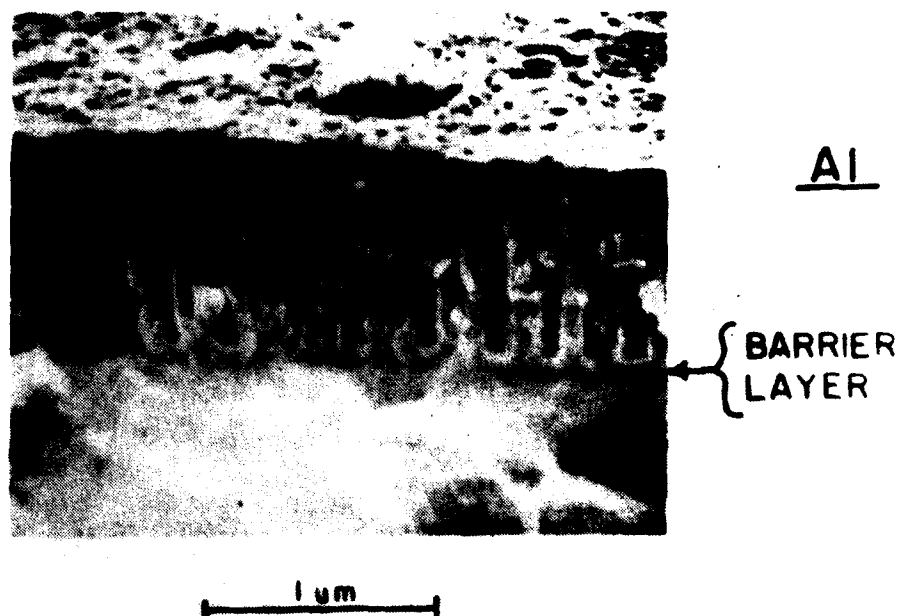
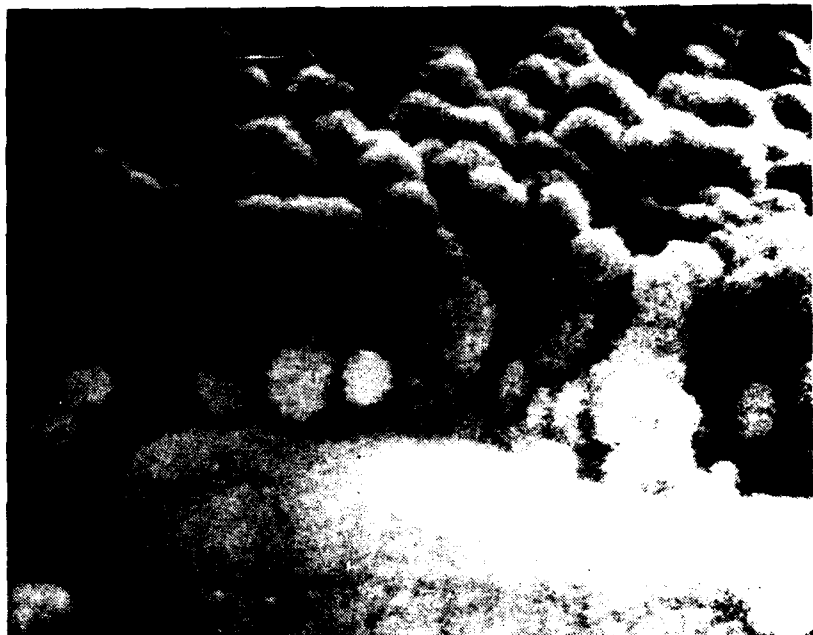
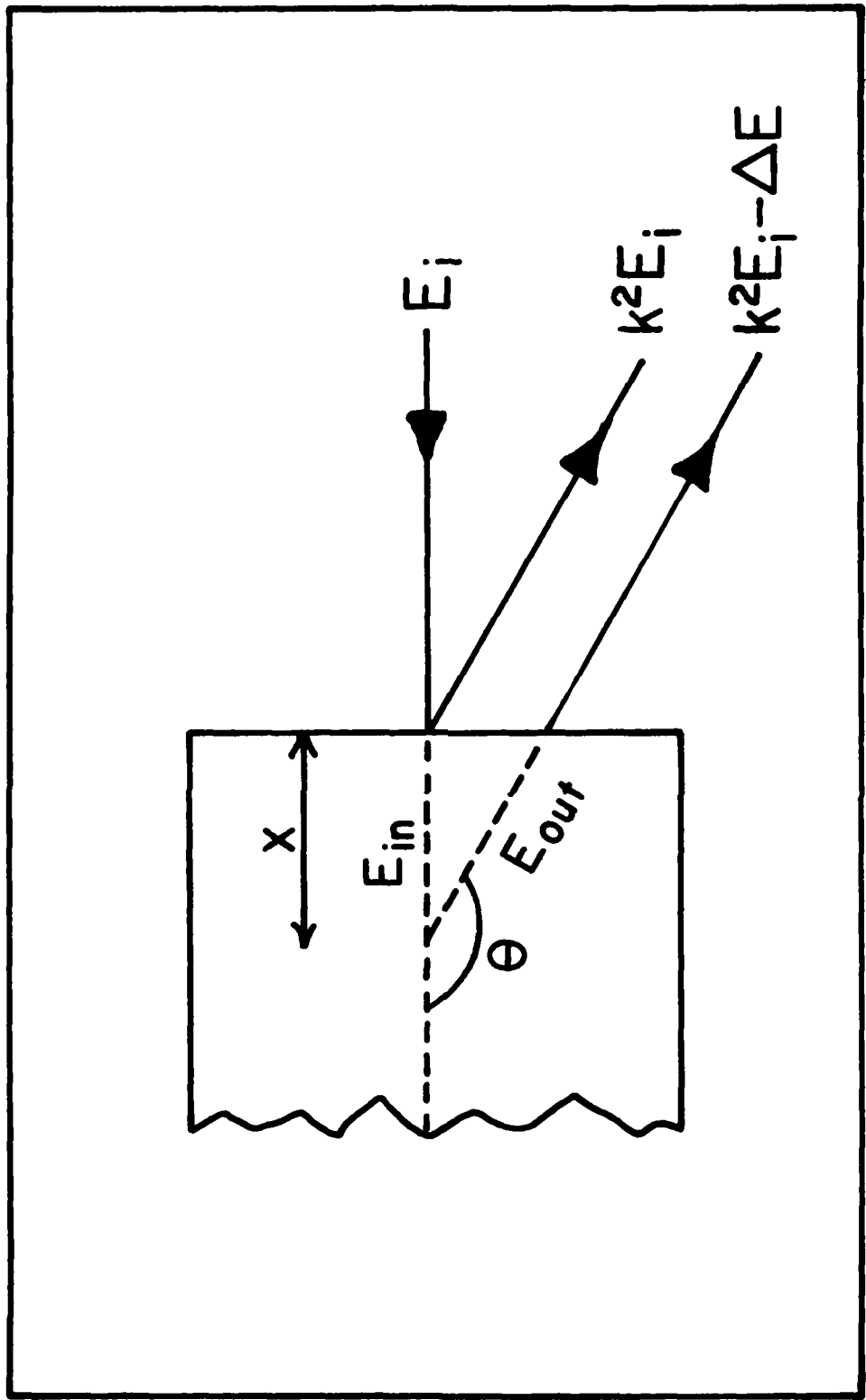


Figure 2 SEM micrograph of oxides on aluminum anodized in room temperature  $0.05M H_3PO_4$  at 60 volts for 1 hour



0.5 $\mu$

Figure 3 SEM micrograph of oxide on 2024-T3 anodized in room temperature 1.0M H<sub>3</sub>PO<sub>4</sub> at 10 volts for 20 minutes



**Figure 4** Illustration of the penetration, backscattering and the subsequent energy loss of a high energy ion in a solid target material

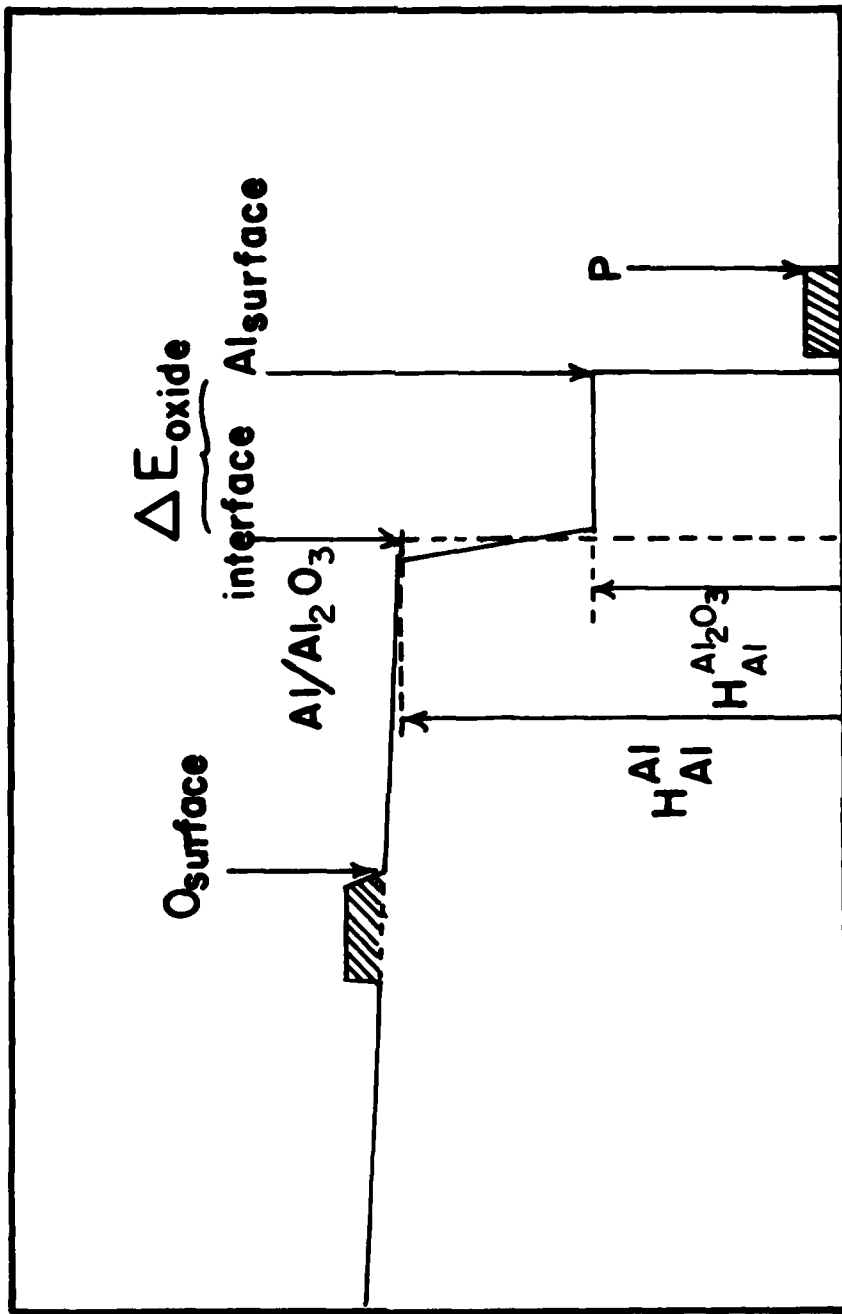


Figure 5 Illustration of an ideal RBS spectrum from a thin anodic oxide on a  $\text{H}_3\text{PO}_4$  anodized aluminum target

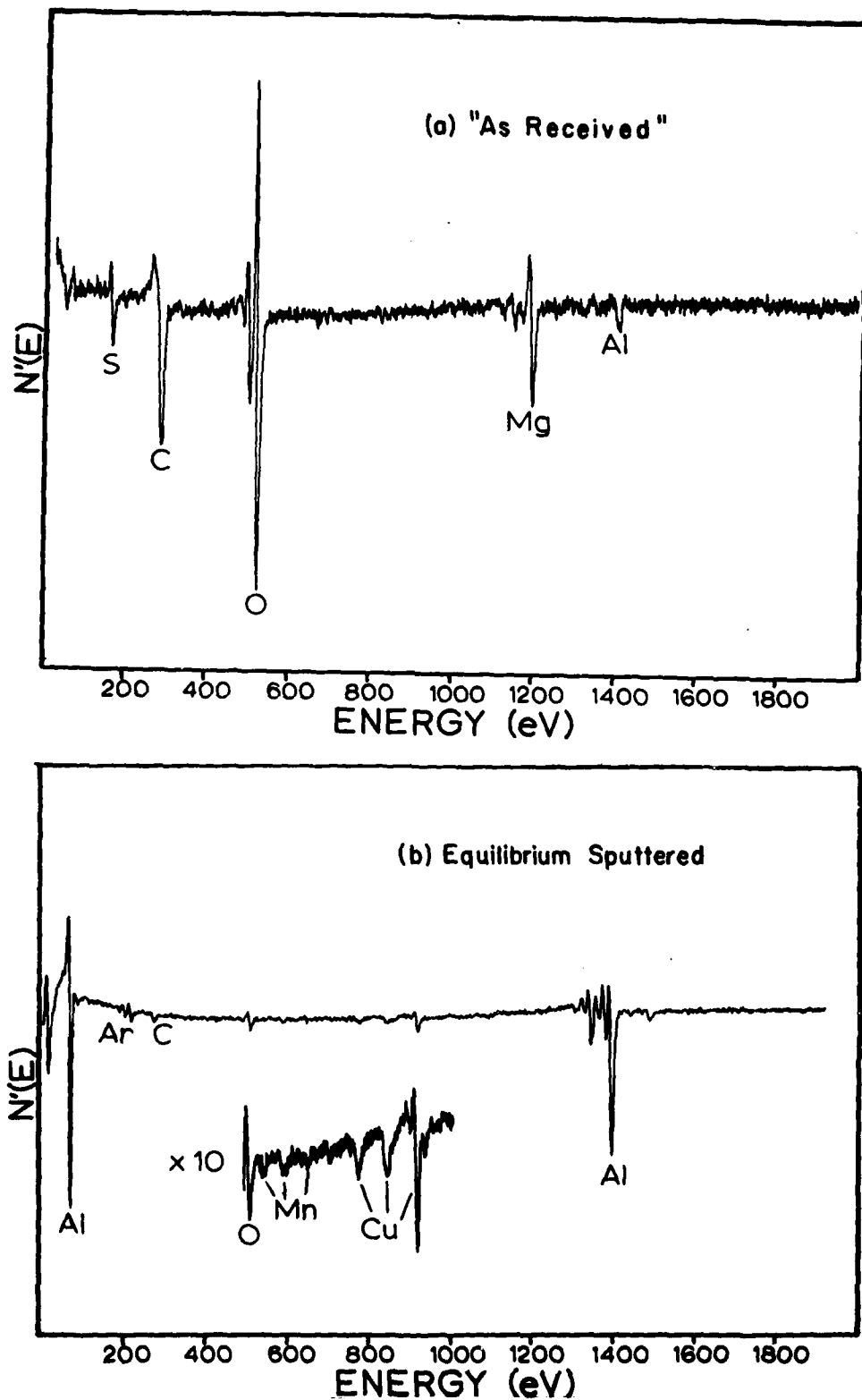


Figure 6 AES spectra of "as received" (a) and equilibrium sputtered (b) 2024-T3 aluminum

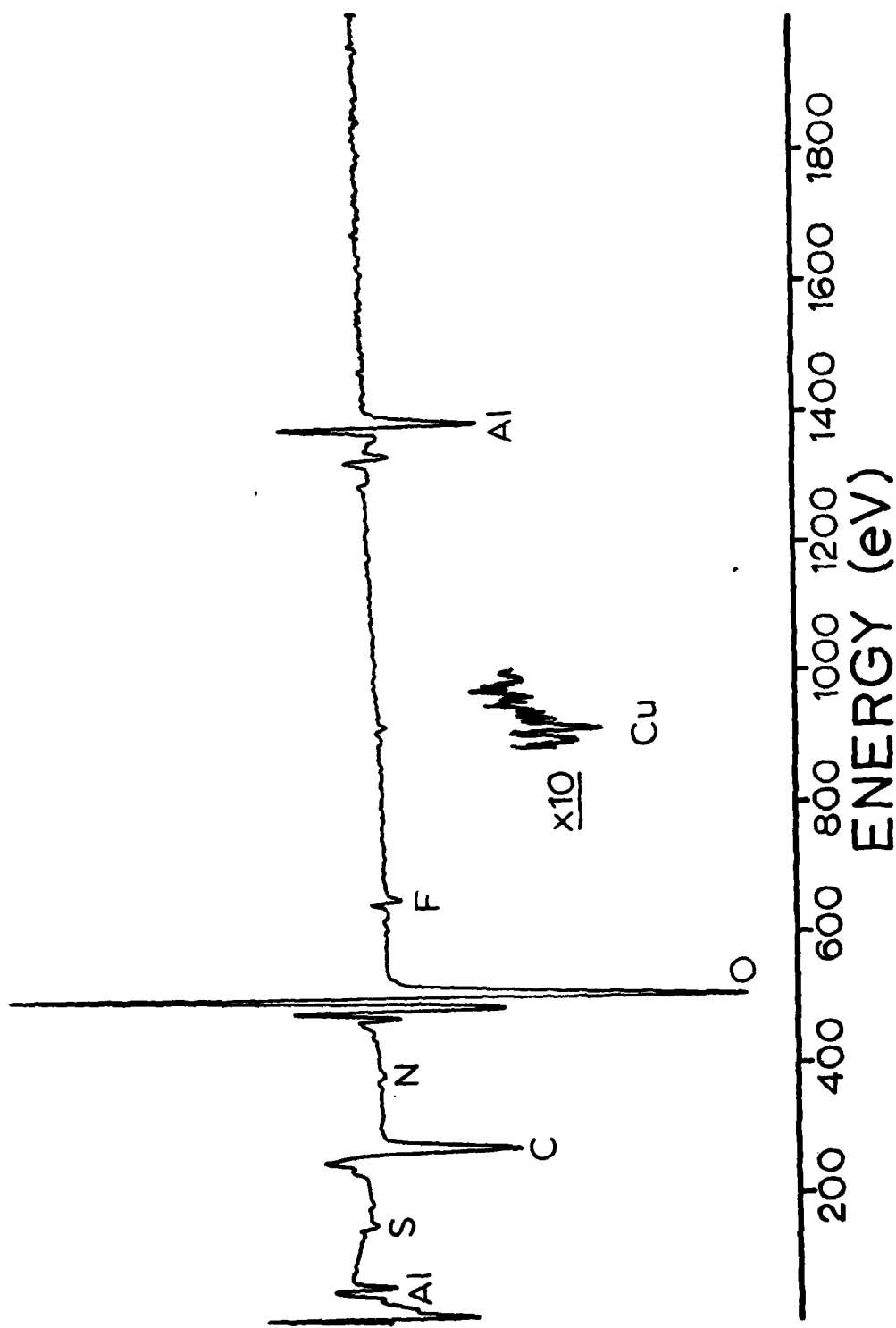


Figure 7 AES spectrum from Oakite-etched 2024-T3 surface

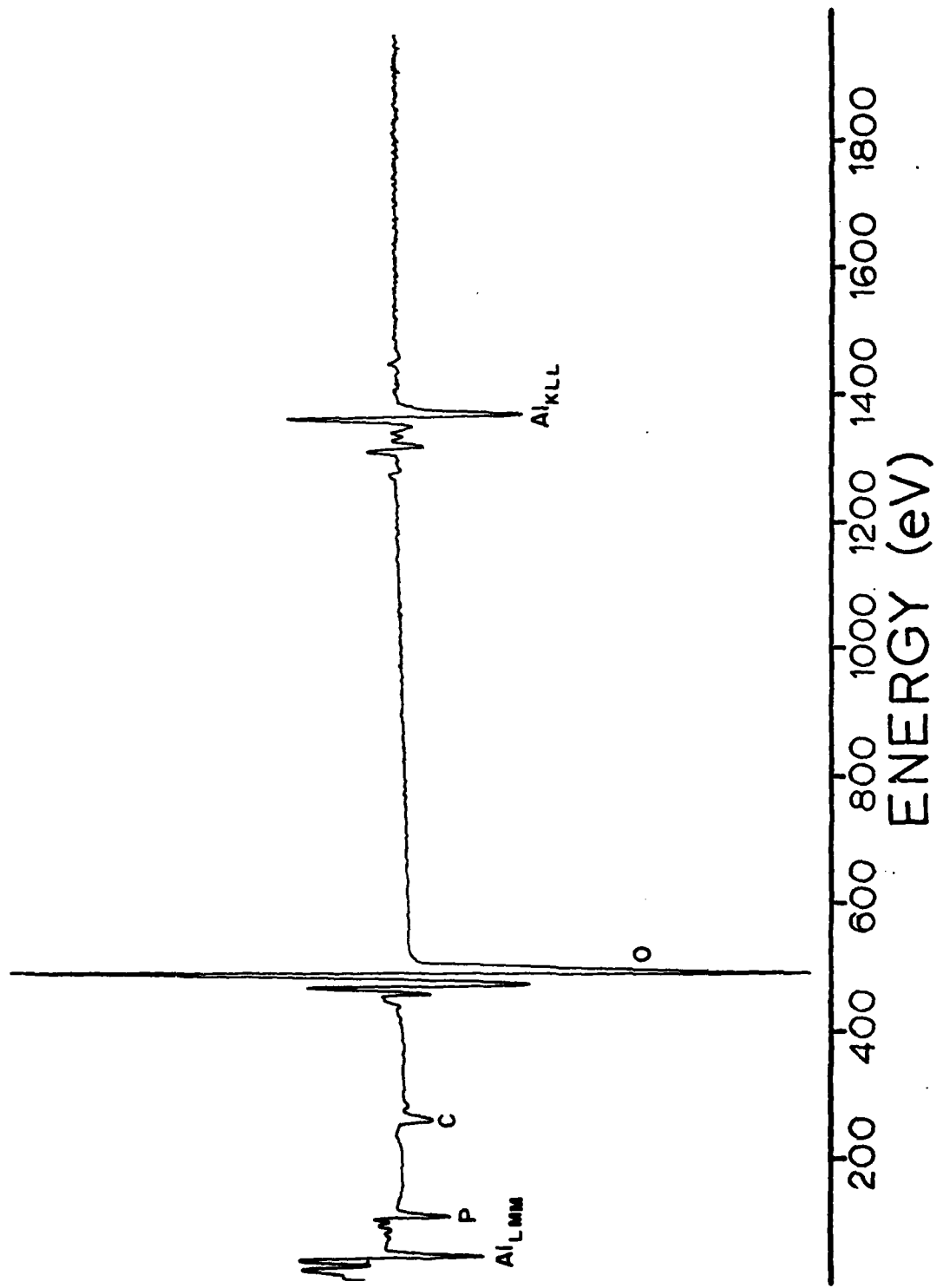


Figure 8 AES spectrum of  $\text{H}_3\text{PO}_4$  anodized 2024-T3

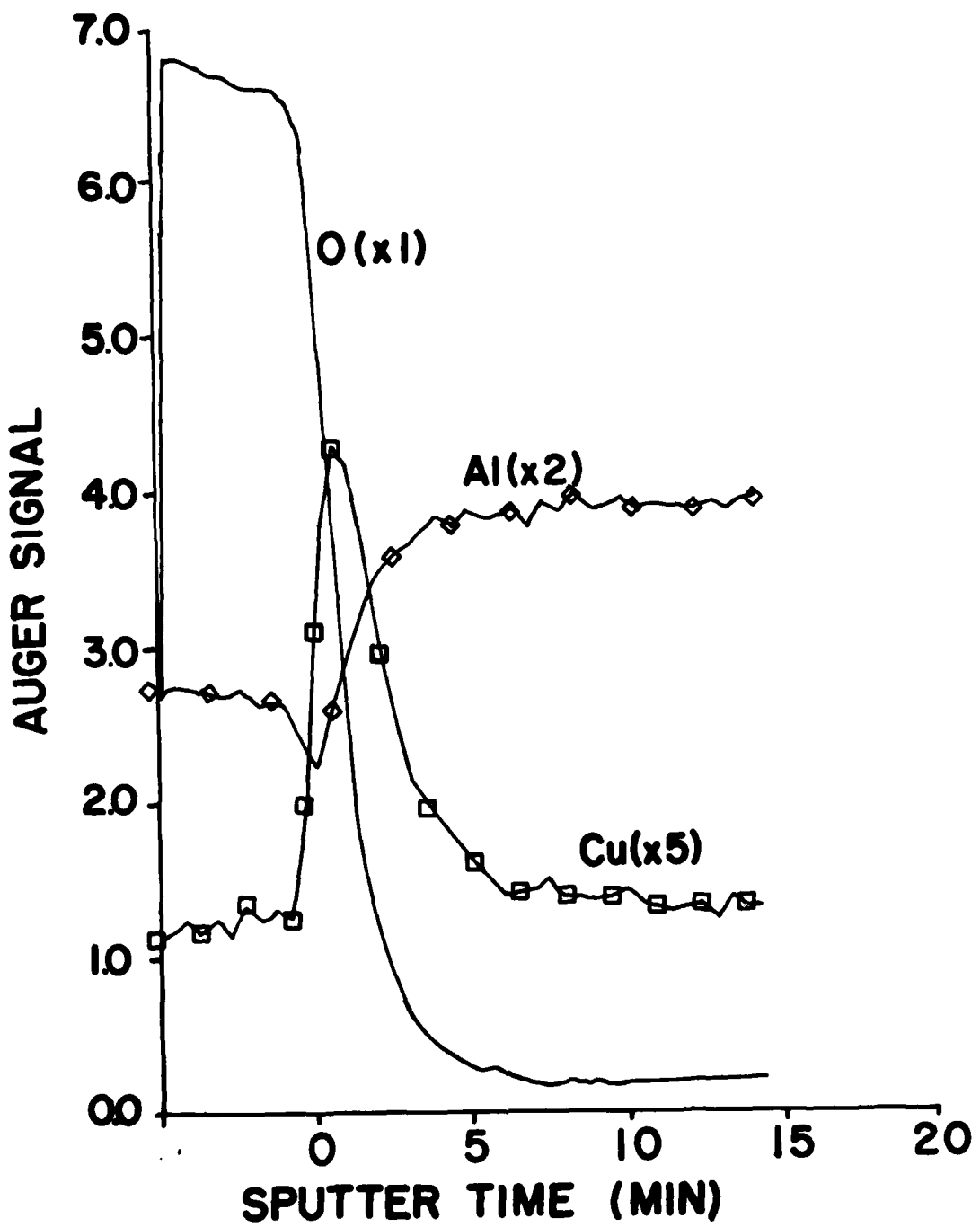


Figure 9 Oxygen, aluminum and copper Auger Sputter profiles of the surface oxide layer of Oakite deoxidized 2024-T3 aluminum

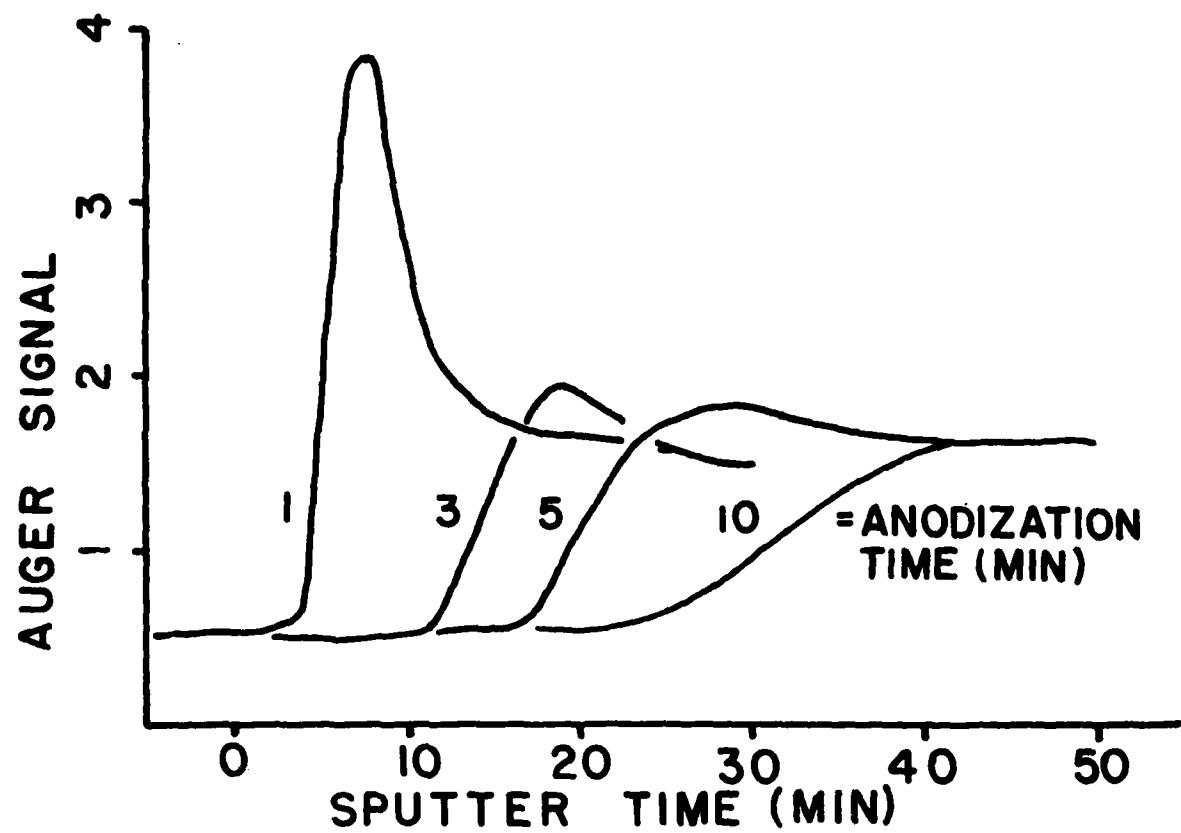


Figure 10 Auger sputter profiles of copper in anodic oxide films on Oakite-etched 2024-T3 anodized at 10 volts in room temperature 1.0M  $H_3PO_4$

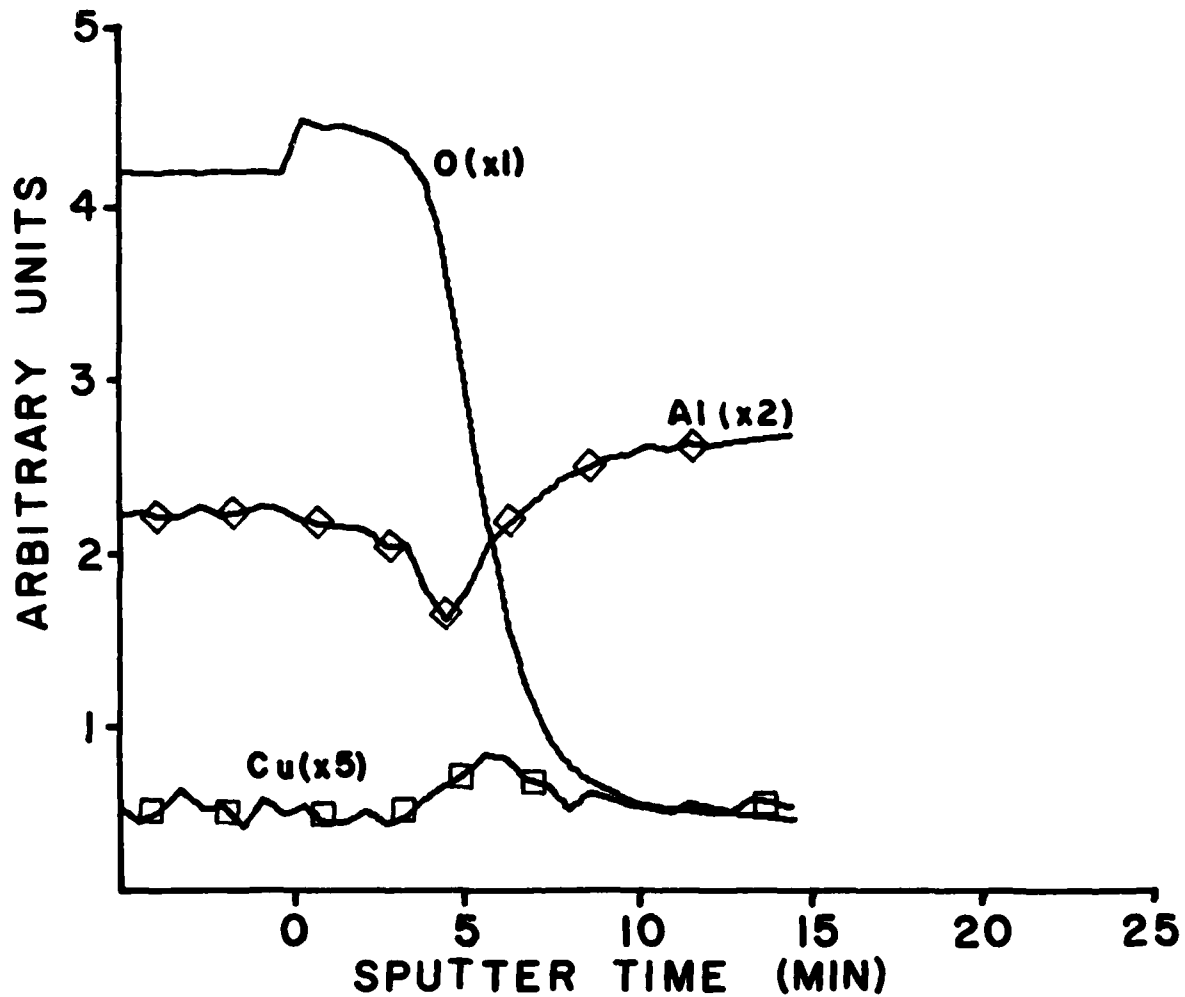


Figure 11 Auger sputter profiles of oxygen, aluminum and copper of the surface oxide layer on non-etched 2024-T3 anodized at 10 volts for 1 minute in room temperature  $1.0M H_3PO_4$

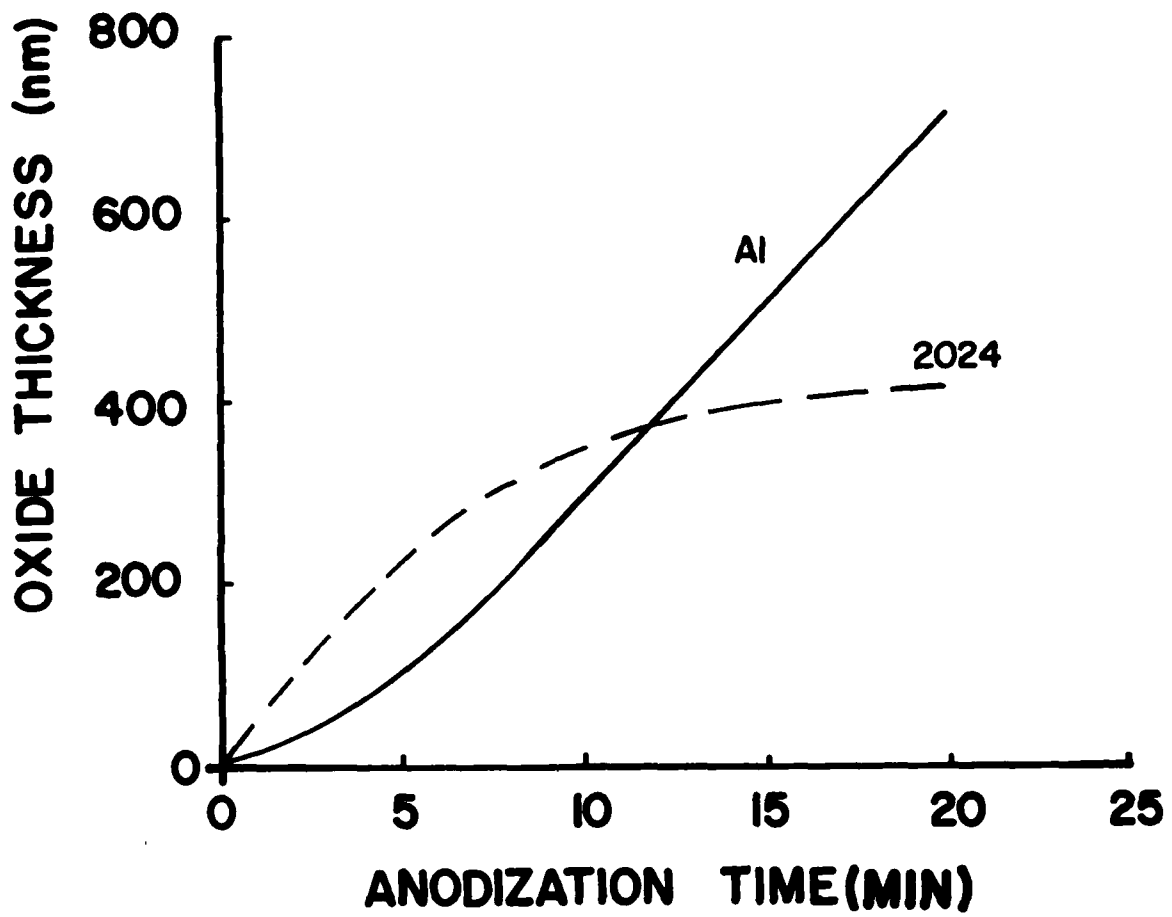


Figure 12 Oxide film thickness on aluminum and 2024-T3 plotted as a function of anodization time at 10 volts in room temperature 1.0M  $H_3PO_4$

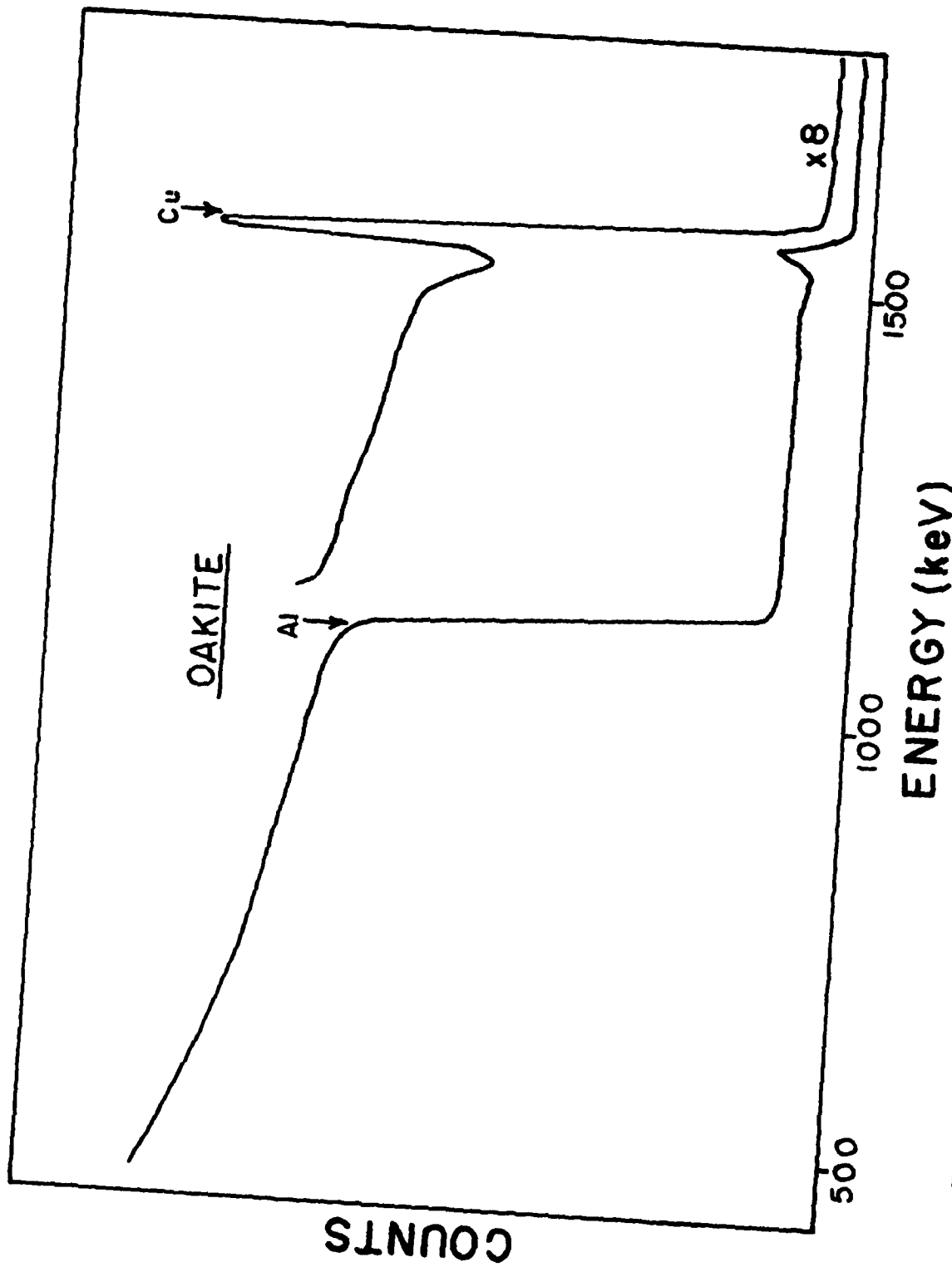


Figure 13 RBS spectrum from Oakite etched 2024-T3 with a 2 MeV  ${}^4\text{He}^+$  beam

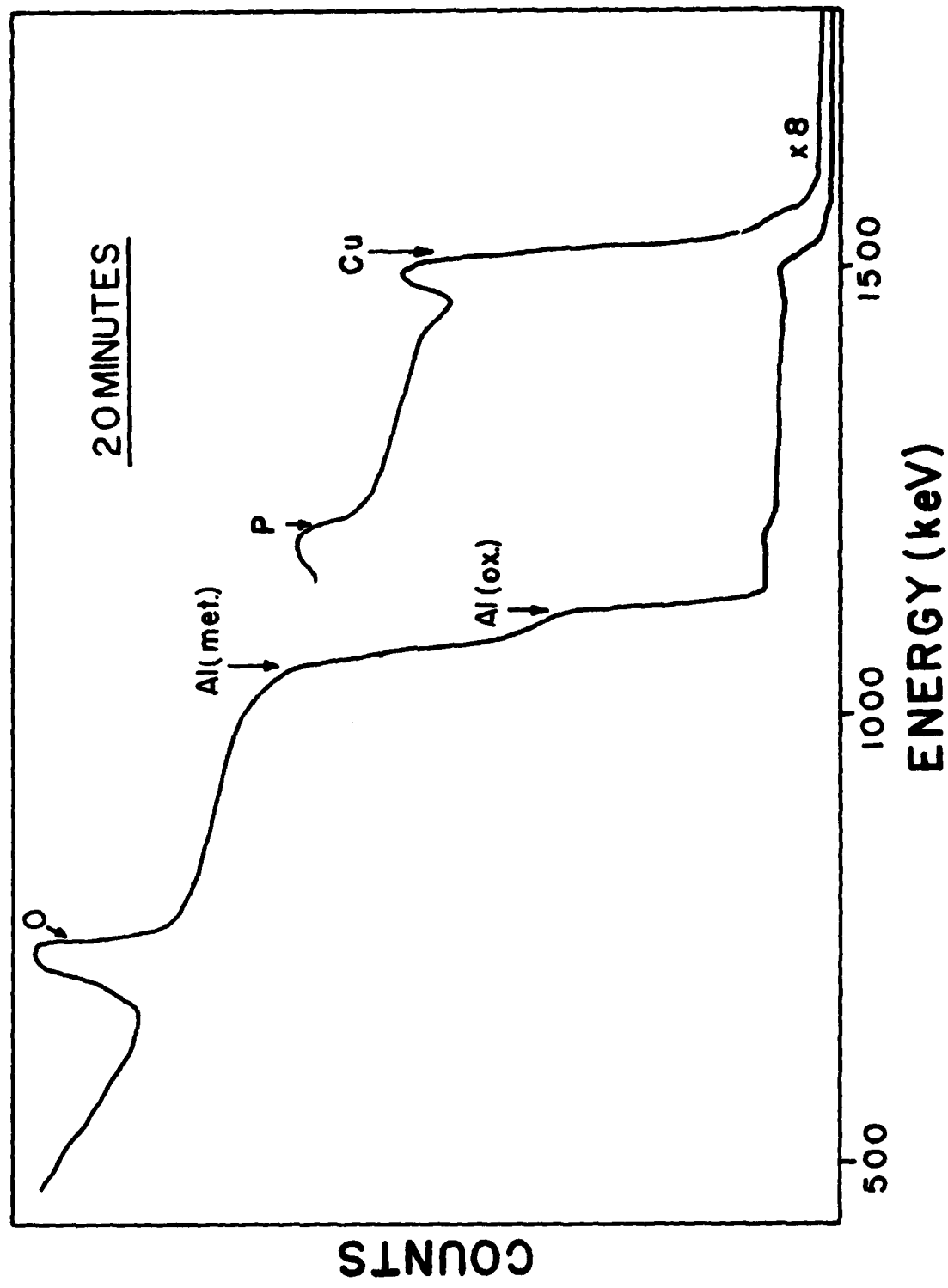


Figure 14 RBS spectrum from Oakite etched 2024-T3 anodized in room temperature 1.0M  $H_3PO_4$  at 10 volts for 20 minutes obtained using a 2 MeV  $^4He^+$  beam

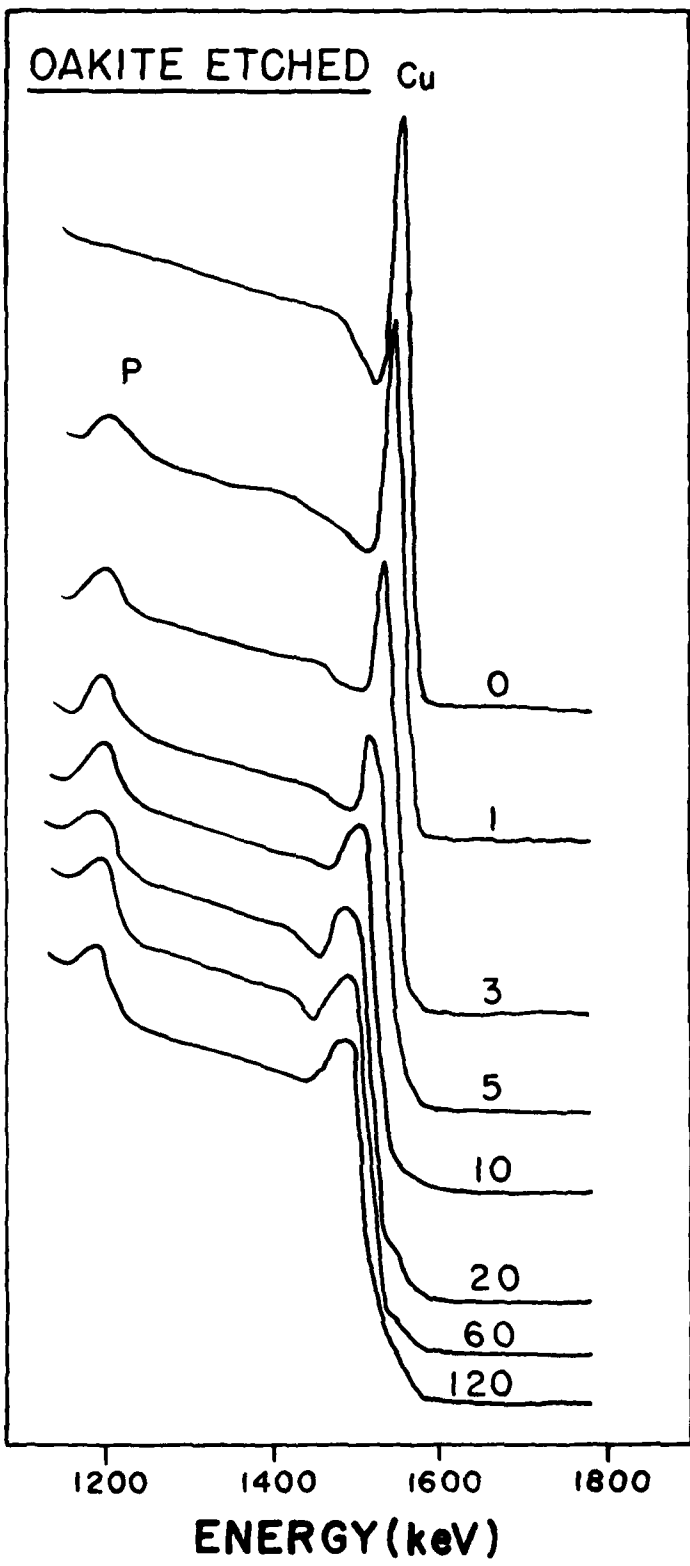


Figure 15 RBS spectra of the Cu and P peaks from Oakite etched 2024-T3 anodized in room temperature 1.0M H<sub>3</sub>PO<sub>4</sub> at 10 volts for times in minutes, as specified for each spectra, using a 2 MeV <sup>4</sup>He beam

**DAT**  
**FILM**